HAL
open science

Fundamentals of metastability exchange optical pumping in helium

Marion Batz, Pierre-Jean Nacher, Geneviève Tastevin

To cite this version:

Marion Batz, Pierre-Jean Nacher, Geneviève Tastevin. Fundamentals of metastability exchange optical pumping in helium. JCNS Workshop on Modern Trends in Production and Applications of Polarized 3He, Jul 2010, Ismaning, Germany. pp.012002, 10.1088/1742-6596/294/1/012002 . hal-00562617v2

HAL Id: hal-00562617

https://hal.science/hal-00562617v2

Submitted on 15 Apr 2011

HAL is a multi-disciplinary open access archive for the deposit and dissemination of scientific research documents, whether they are published or not. The documents may come from teaching and research institutions in France or abroad, or from public or private research centers.

L'archive ouverte pluridisciplinaire **HAL**, est destinée au dépôt et à la diffusion de documents scientifiques de niveau recherche, publiés ou non, émanant des établissements d'enseignement et de recherche français ou étrangers, des laboratoires publics ou privés.

Preprint - April 2011 *To be published in Journal of Physics: Conference Series*

Fundamentals of metastability exchange optical pumping in helium

Marion Batz[1,2], Pierre-Jean Nacher[1] and Geneviève Tastevin[1]

Abstract. Advances in metastability exchange optical pumping (MEOP) at high laser powers, but also at high gas pressures and high magnetic field strengths, has provided strong motivation for revisiting the understanding of the limitations of this powerful technique. A comprehensive model has been developped for improved description of the combined effects of OP, ME, and relaxation, and of detailed MEOP features observed over the broad range of operating conditions. A brief description is provided, with illustrative comparisons of computed and experimental results. This improved tool is used to explain the excellent photon efficiency of OP obtained at all field strengths. It is combined with an angular momentum budget approach to quantitatively investigate the newly discovered strong OP-enhanced polarisation losses that currently limits MEOP performance.

[1] Laboratoire Kastler Brossel, ENS; CNRS; UPMC; 24 rue Lhomond, F-75005 Paris, France.
[2] Johannes Gutenberg University, Staudingerweg 7, D 55128 Mainz, Germany.

E-mail: `nacher@lkb.ens.fr`

1. Introduction

Metastability exchange optical pumping (MEOP), discovered in 1963 [1], exclusively applies to ^{3}He as demonstrated by various attempts for other gases [2, 3, 4], while spin-exchange OP (that involves an alkali vapour [5, 6, 7]) can be used to efficiently polarise ^{129}Xe as well. MEOP is actually performed between two excited states of helium (Fig. 1). The 2^3S metastable state, that plays the role of a ground state for the OP process, is populated by electron collisions in a plasma discharge sustained in a gas at moderate pressure (usually up to a few millibars). For the ^{3}He isotope in this excited metastable state, an efficient coupling between the nucleus and the electrons (the hyperfine interaction) results in a strong entanglement of electronic and nuclear spin states. Therefore the OP-enforced optical orientation of the electronic angular momentum simultaneously induces nuclear orientation as well. This nuclear orientation is transferred through metastability exchange collisions to the much more numerous atoms having remained in the true (1^1S_0) ground state.

When laser light with adequate spectral characteristics at 1083 nm is used, MEOP provides very high nuclear polarisation (>0.7) with good photon efficiency (∼1 polarised nucleus per absorbed photon) [8]. Given the development of suitable high power fibre lasers [9, 10, 11], the only drawback of this method is the limited range of operating pressures (of order 0.5-5 mbar [12]) for which a suitable plasma can excite metastable atoms. When a higher final pressure is needed, non-relaxing compression of the gas becomes necessary and this introduces demanding requirements on the gas handling and compressing devices. However it has recently been shown that the range of operating pressures can be extended to several tens or hundreds of mbar by performing MEOP in a high magnetic field, such as the 1.5 T field of a magnetic resonance

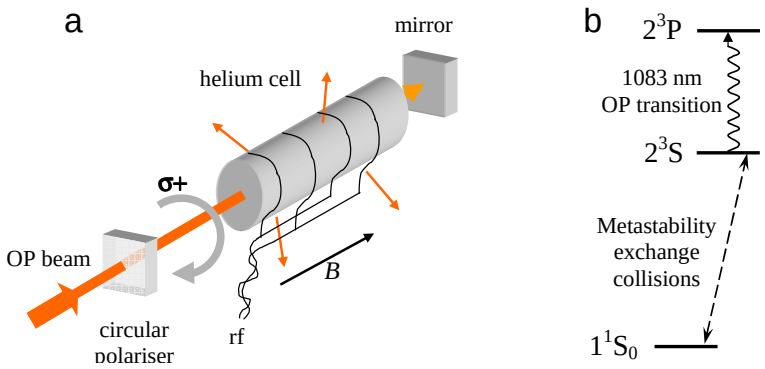

Figure 1. a: Schematic view of a basic MEOP set-up. In a ^{3}He gas cell, a weak rf discharge promotes a small fraction of the atoms into the excited metastable state 2^3S, where resonant absorption of 1083 nm light occurs. This OP light is circularly polarised and propagates along the direction of the applied magnetic field B. For enhanced absorption, the light is usually back-reflected for a second pass through the cell. Nuclear polarisation is transferred to atoms in the ground state by metastability exchange collisions. **b:** The atomic levels of He and the main physical processes involved in MEOP are shown. The 2^3S and 2^3P states are composed of several levels and the 1083 nm line thus has a complex structure (see Fig. 2).

imaging (MRI) system [13, 14], and up to 4.7 T [15]. Operating at higher pressures would make subsequent compression significantly easier to perform.

The first theoretical articles on MEOP were written in the 1970s [1, 16, 17, 18, 19]. At that time, OP on the 2^3S-2^3P transition was performed using the weak light from a helium lamp and rather low polarisations (of the order of 0.1) were obtained. Simple linearised models were sufficient to account for such pumping experiments. When laser sources at 1083 nm were developed in the 1980s, much higher nuclear polarisations were obtained. A detailed model for MEOP without restriction on the pump light intensity nor on the nuclear polarisation was then proposed [8]. It is based on rate equations for the populations of the 2^3S, 2^3P, and ground states, that accurately take into account the effects of metastability exchange collisions and of absorption and emission of light at 1083 nm. Correlations between atomic orientations and velocities, created for instance by a spectrally narrow laser in a room temperature gas, are also considered in this model, but only in a crude phenomenological way. This model only describes low field MEOP and it has been established and used for parameters corresponding to low pressure situations (in the mbar range) where MEOP was known to have the highest efficiency. This model has been also used to discuss OP experiments with a broadband laser [20, 21]. Extensions to specific situations have been proposed, but not fully developed, for OP in ^{3}He-^{4}He isotopic mixtures[1] [23] and for OP in high magnetic fields [12, 13, 24]. Recently, we have developed a more comprehensive model of MEOP. It is based on similar rate equations for the populations of all Zeeman sublevels but it is suitable for arbitrary magnetic field and for pure ^{3}He gas as well as for isotopic gas mixtures. It provides a unified frame that is also more adequate for description of MEOP with modern, broadband fibre lasers.

The main features of this improved model are described in section 2, where it is simply used as a tool to illustrate the combined effects of ME, OP, and relaxation for conditions typically met in MEOP-based ^{3}He gas polarisers. Section 3 is devoted to a more global discussion of the net growth rate of ^{3}He nuclear polarisation in the ground state, through an angular momentum

[1] OP performed on the 2^3S state of ^{4}He atoms in an isotopic mixture is an efficient scheme providing high ^{3}He nuclear polarisations [10, 22]. It can be advantageoulsly used when the presence of ^{4}He is desired or is not a nuisance, e.g., for low temperature studies of polarised mixtures or for neutron spin filters applications.

budget that combines the photon efficiency of the 2^3S-2^3P transition and a total polarisation loss that only involves 2^3S and ground state relaxation rates. Section 4 provides an example of experimental implementation and of analysis of polarisation dynamics for systematic MEOP study at low field. Comparison of measured and computed polarisations provides a clear evidence of a strong laser-induced relaxation rate that scales linearly with the absorbed light power.

2. Main features of the comprehensive MEOP model

The key processes in MEOP are the net transfer of angular momentum from absorbed light to spin degrees of freedom of He atoms (in the 2^3S and 2^3P states) and the transfer of nuclear angular momentum between ground state ^{3}He atoms and atoms in the 2^3S state by metastability exchange collisions. A detailed balance with the angular momentum losses resulting from various relaxation processes is used to derive rate equations for the relevant populations: $(1 \pm M)/2$ for the two Zeeman sublevels (m_I=$\pm$1/2) of the ground state of ^{3}He atoms, characterised by its nuclear polarisation M, the populations of the 2^3S metastable state and those of the 2^3P state.

2.1. Level structure of the 2^3S and 2^3P states

We use the notations of reference [24] where the structure and energies of the sublevels of the 2^3S and 2^3P states are derived for both isotopes in arbitrary magnetic field. For simplicity we only discuss two experimentally relevant limiting cases: low and high magnetic fields.

2.1.1. Low field - The 2^3S state of ^{4}He has three magnetic sublevels (m_S=-1, 0, and 1), linearly split at all values of the applied magnetic field B by the Zeeman energy. They are named Y_1 to Y_3 and their populations y_1 to y_3 (for all sets of populations, indices increase with increasing energies). The 2^3P state of ^{4}He has three fine-structure levels with J=0, 1 and 2 (see Fig 2a), hence nine Zeeman sublevels. There are twice as many Zeeman sublevels for ^{3}He due to its two nuclear spin states: six (A_1 to A_6, populations a_1 to a_6) in the 2^3S state and eighteen (B_1 to B_{18}, populations[2] b_1 to b_{18}) in the 2^3P state that has five fine- and hyperfine-structure levels (see Fig 2b). In low magnetic field, the F=3/2 and F=1/2 hyperfine levels of the 2^3S state of ^{3}He are well resolved and split by 6.74 GHz (Fig 2b). The magnetic sublevels can be written using the decoupled basis states $|m_S, m_I\rangle$. A_1=$|-1,-\rangle$ and A_4=$|1,+\rangle$ are pure states of maximum $|m_F|$=3/2 but the other states involve large mixing parameters θ_- and θ_+ [24]:

$$\begin{aligned}
A_2 &= \cos\theta_- \,|-1,+\rangle + \sin\theta_- \,|0,-\rangle \\
A_3 &= \cos\theta_+ \,|0,+\rangle + \sin\theta_+ \,|1,-\rangle \\
A_5 &= \cos\theta_- \,|0,-\rangle - \sin\theta_- \,|-1,+\rangle \\
A_6 &= \cos\theta_+ \,|1,-\rangle - \sin\theta_+ \,|0,+\rangle \,. \qquad (1)
\end{aligned}$$

Strong and maximal mixing of electronic and nuclear angular momenta occurs at B=0, with $\sin^2\theta_-$=2/3 and $\sin^2\theta_+$=1/3. The mixing parameters and the sublevel energies, as well as those of the 2^3P_0 sublevels addressed by the C_8 and C_9 transitions used for ^{3}He MEOP (see Fig 2b), linearly depend on B for low fields. The corresponding Zeeman line shifts do not exceed 30 MHz/mT and the relative changes in transition intensities do not exceed 0.6 %/mT. Given the Doppler width of the optical transitions (of order 2 GHz fwhm at room temperature for ^{3}He), the OP rate equations are almost field-independent up to several mT.

[2] The local number density of 2^3S atoms in sublevel A_i is $n_m a_i$ (n_m is the number density of atoms in the metastable state and the a_is are populations such that $\sum_{i=1}^{6} a_i$=1). For convenience, the b_js are defined so that the number density of atoms in sublevel B_j of the 2^3P state is $n_m b_j$. Hence the b_js are not true populations, and $\sum_{k=1}^{18} b_k$<1 depends on the OP light intensity.

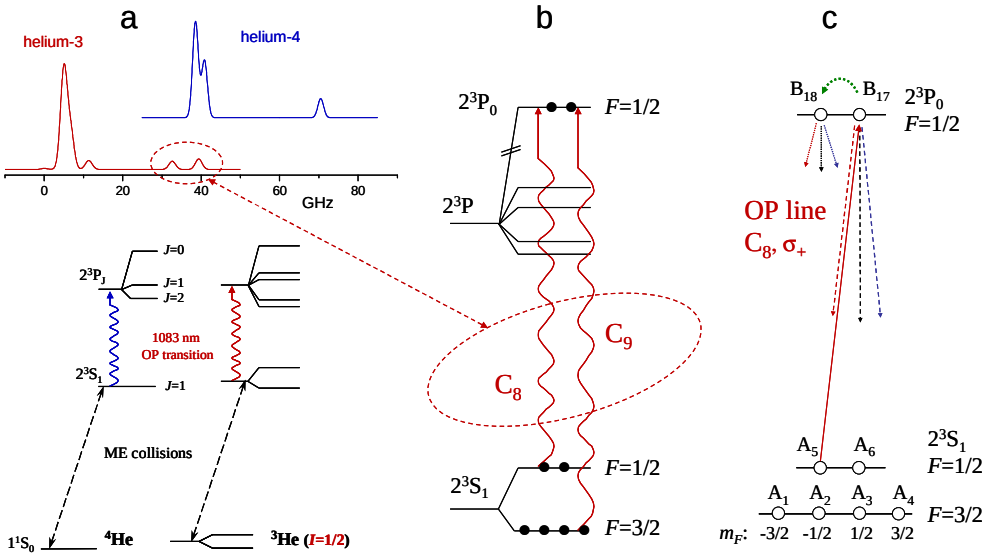

Figure 2. a: Fine- and hyperfine-structures of the atomic states of He involved in the MEOP process, for the ^{4}He (left) and ^{3}He (right) isotopes, in low magnetic field (below a few 10 mT). The resulting spectra of the 1083 nm transition (upper graphs, computed with 300 K Doppler widths and no collisional broadening) extend over ~70 GHz when the isotope shift is considered. Optical transition frequencies are referenced to that of the C_1 line at zero field [24]. **b:** C_8 and C_9 lines, which are the most efficient in usual OP conditions, connect the 2^3S_1, F=1/2 and F=3/2 levels of ^{3}He, respectively, to the 2^3P_0 level. **c:** Example of elementary processes considered in the angular momentum budget for C_8 OP (see text).

2.1.2. High field - When the Zeeman energy exceeds the fine- and hyperfine-structure energy scales the angular momentum structures of 2^3S and 2^3P levels and the 1083 nm transition are deeply modified. Figure 3 displays the energy of all Zeeman sublevels for B=1.5 T, a field strength commonly met in MRI systems and thus of practical importance for applications to human lung MRI using polarised ^{3}He gas. At this field strength, only a weak state mixing remains in the 2^3S state (Eqs. 1 with $\sin\theta_+$=0.07128 and $\sin\theta_-$=0.07697). The six Zeeman sublevels of the ^{3}He isotope levels are organised in three pairs of states (Fig. 3, left bottom graph). In each pair the level energy is mostly determined by the common dominant value of m_S (compare with Fig. 3, right bottom graph) while the nuclear spin projections are almost antiparallel. Similarly, hyperfine coupling only weakly mixes levels of different m_I values in the 2^3P state (Fig. 3, upper left graph). As a result, high-field spectra for a given light polarisation are thus composed of six main components which appear in two groups: a pair and a quartet, each group being unresolved at room temperature. These features clearly appear on the ^{3}He absorption spectra displayed in Fig. 4, that are computed at 1.5 T assuming room temperature Doppler widths and no collision broadening. The strong lines in the ^{3}He spectra are labelled $f_n^{\pm}$, where n=2 or 4 refers to the number of unresolved components and $\pm$ to the sign of the circular light polarisation. Weaker doublets of resolved single-component lines of interest for optical detection purpose are highlighted (two options exist for σ_+ polarisation). They separately address sublevels A_1 and A_2 (resp. A_5 and A_6) for σ_+ (resp. σ_-) polarised light.

2.2. Metastability exchange and spin-temperature distribution

An important feature of metastability exchange collisions in helium is that negligible depolarisation occurs during the collisions, due to the fact that all involved angular momenta

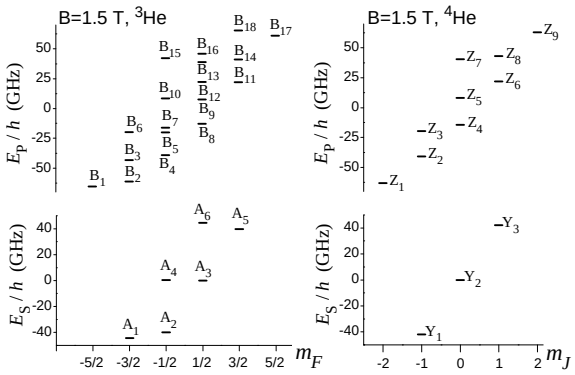

Figure 3. Energies (E_S/h and E_P/h, in frequency units) and angular momentum projections (m_F or m_J) of the sublevels of the 2^3S and 2^3P states of ^{3}He (left) and ^{4}He (right) at 1.5 Tesla. Energy references and state labelling are identical to those of [24].

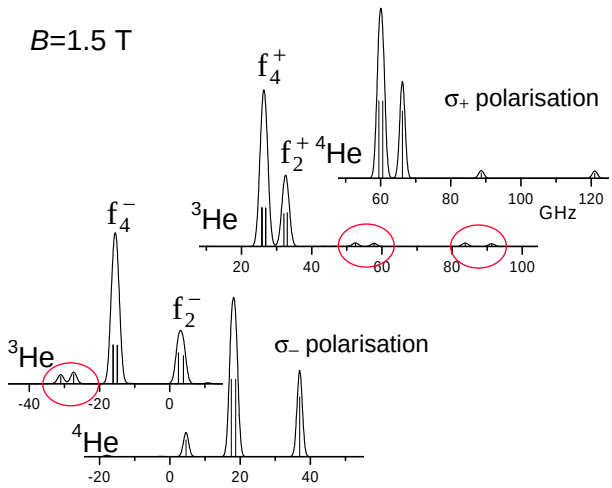

Figure 4. 1083 nm absorption spectra of ^{3}He and ^{4}He at 1.5 T for circularly polarised light. Optical transition frequencies are referenced to that of the C_1 line in zero field [24]. Pump and probe lines relevant for high field MEOP are described in text.

are spins [25]. Introducing density operators $\rho_{\rm g}$ and $\rho_{\rm m}$ to characterise the spin states of colliding ground state and metastable state atoms, respectively, a ME collision where excitation is exchanged between colliding atoms can be described as:

$$\begin{array}{ccccccc} \text{He} & + & \text{He}^* & \rightarrow & \text{He}^* & + & \text{He} \\ \rho_{\rm g} & & \rho_{\rm m} & & \rho'_{\rm g} & & \rho'_{\rm m}. \end{array} \tag{2}$$

All relevant collisions between ^{3}He and ^{4}He atoms occuring in isotopic mixtures are discussed in reference [24]. In pure ^{3}He, one simply has just before a collision:

$$\rho_{\rm g} = \frac{1+M}{2}\left|+\right\rangle\left\langle+\right| + \frac{1-M}{2}\left|-\right\rangle\left\langle-\right| \quad \text{and} \quad \rho_{\rm m} = \sum\nolimits_1^6 a_i \left|{\rm A}_i\right\rangle\left\langle{\rm A}_i\right|, \tag{3}$$

and just after ME collision:

$$\rho'_{\rm g} = {\rm Tr}_e\, \rho_{\rm m} \quad \text{and} \quad \rho'_{\rm m} = \rho_g \otimes {\rm Tr}_n\, \rho_{\rm m} \tag{4}$$

where ${\rm Tr}_e$, ${\rm Tr}_n$ are trace operators over the electronic and nuclear variables respectively [19]. Indeed, $\rho'_{\rm m}$ contains off-diagonal terms and has to be projected on the eigenstates ${\rm A}_i$ to derive rate equations for the populations. These equations explicitly depend linearly on M due to the linear dependence of $\rho_{\rm g}$ on M in Eq. 4. For pure ^{3}He they reduce to:

$$\left.\frac{da_i}{dt}\right|_{\rm ME} = \gamma_{\rm e}\left(-a_i + \sum_{k=1}^{6}(E^3_{ik} + MF^3_{ik})a_k\right). \tag{5}$$

The ME collision rate $\gamma_{\rm e}$ is proportional to gas pressure (3.75×10^6 s^{-1}/mbar in pure ^{3}He [26]). The B-dependent matrices E^3 and F^3 involve the mixing parameters θ_+ and θ_- of Eqs. 1 [24]. Given the decreasing values of these parameters at high B, several elements in the matrices decrease so as to only leave weaker couplings of order $\theta^2_\pm$. However, the ME collision rate is

increased at high pressures and this advantageously compensates for the weaker couplings in the ME rate equations.

It can be shown that the populations of the sublevels that are coupled by ME collisions follow a Boltzmann-like distribution of angular momenta in all situations where OP and relaxation processes have negligible effect on populations. This is valid at all field strengths, and for pure ^{3}He as well as for isotopic mixtures [24]. Since number densities n_m of atoms in the metastable state are much lower than the ground state number density N_g (typically, $n_\mathrm{m}/N_\mathrm{g} \sim 10^{-6}$), the spin temperature (ST) of this distribution is controlled by the nuclear polarisation M. Noting e^β the ratio $(1+M)/(1-M)$ of the populations in the ground state ($1/\beta$ is the ST), the populations a_i^ST and y_i^ST are given by [24]:

$$a_i^\mathrm{ST} = e^{\beta m_\mathrm{F}}/(e^{3\beta/2} + 2e^{\beta/2} + 2e^{-\beta/2} + e^{-3\beta/2}) \quad \text{for } ^3\mathrm{He}, \tag{6}$$

$$y_i^\mathrm{ST} = e^{\beta m_\mathrm{S}}/(e^{\beta} + 1 + e^{-\beta}) \quad \text{for } ^4\mathrm{He}, \tag{7}$$

where m_F and m_S are the relevant angular momentum projections. The ST populations can alternatively be expressed as functions of M. The following formulas are valid up to B=0.1619 T:

$$a_1^\mathrm{ST} = \frac{(1-M)^3}{2M^2+6},\ a_4^\mathrm{ST} = \frac{(1+M)^3}{2M^2+6} \quad \text{for } ^3\mathrm{He},\ m_F = \mp 3/2, \tag{8}$$

$$a_2^\mathrm{ST} = a_5^\mathrm{ST} = \frac{(1-M)^2(1+M)}{2M^2+6},\ a_3^\mathrm{ST} = a_6^\mathrm{ST} = \frac{(1-M)(1+M)^2}{2M^2+6} \quad \text{for } ^3\mathrm{He},\ m_F = \mp 1/2, \tag{9}$$

$$y_1^\mathrm{ST} = \frac{(1-M)^2}{M^2+3},\ y_2^\mathrm{ST} = \frac{1-M^2}{M^2+3},\ \text{and}\ y_3^\mathrm{ST} = \frac{(1+M)^2}{M^2+3} \quad \text{for } ^4\mathrm{He},\ m_J = -1,\ 0,\ \text{and } 1. \tag{10}$$

Level crossings (A_4 and A_5 at 0.1619 T, A_3 and A_4 at 4.716 T [24]) simply result in the corresponding permutation of indices in Eqs. 8 and 9 at high field strengths.

The spin-temperature distribution of populations at given ground state polarisation is affected by two competing processes: relaxation in the 2^3S state, that tends to equalise all populations, and OP, that tends to deplete the sublevels addressed by the optical transitions. They are now briefly discussed for MEOP in pure ^{3}He gas.

2.3. Relaxation processes

Relaxation phenomenologically describes the effect of additional processes that couple populations of different sublevels. They involve very different time scales in the two excited states:

In the 2^3S state, collisions do not affect the orbital angular momentum L=0 and only couple populations through spin exchange (i.e., through ME that conserves angular momentum and gives rise to the contribution described by Eq. 5). Relaxation is thus usually rather slow, associated for instance with de-excitation of the atom and re-excitation in the plasma. The effect of this process on ^{3}He populations is taken into account in the MEOP model through:

$$\left.\frac{da_i}{dt}\right|_\mathrm{r} = \gamma_\mathrm{r}^\mathrm{S}\left(\frac{1}{6} - a_i\right). \tag{11}$$

Depending on pressure, cell dimensions, gas purity, etc., the relaxation rate $\gamma_\mathrm{r}^\mathrm{S}$ is typically of order 10^3 s^{-1} in the 2^3S state. A lower bound is set by de-excitation on the cell wall, which involves diffusion of metastable atoms in the gas (with a diffusion coefficient given in [27]).

In contrast, in the 2^3P state, J-changing collisions occur at a much higher rate, proportional to pressure and of order a few 10^7s^{-1}/mbar [28, 29]. This can result in significant population

transfers during the 2^3P state radiative lifetime. They are phenomenologically described in the MEOP model by a single relaxation rate $\gamma_{\rm r}^{\rm P}$ and by rate equations:[3]

$$\left.\frac{db_j}{dt}\right|_{\rm r} = \gamma_{\rm r}^{\rm P}\left(\frac{1}{18}\sum\nolimits_{k=1}^{18} b_k - b_j\right). \tag{12}$$

The 2^3P relaxation rate $\gamma_{\rm r}^{\rm P}$ is expected to also scale with pressure p, and the value $\gamma_{\rm r}^{\rm P}/p$=0.32×10^7 s^{-1}/mbar has been recently inferred from OP efficiency measurements [30].

Equations similar to Eqs. 11 and 12 are given in [24] for the populations of ^{4}He atoms involved in MEOP of isotopic mixtures.

In high magnetic field, due to the deep change in the structure of the 2^3P state sublevels, this description using a single relaxation rate may be questioned. However, for MEOP at high enough pressure, fast redistribution among sublevels can be assumed to fully equalise the populations and a simplified model can be used (see [31] and Sec. 2.4).

2.4. OP processes - A two-class MEOP model

OP promotes atoms from selected Zeeman sublevels of the 2^3S state to sublevels of the 2^3P state. For instance, for the simple low-field case illustrated in Fig 2c, the C_8 line with right-handed circular (σ_+) polarisation excites atoms from the A_5 sublevel (m_F=-1/2) to the B_{17} sublevel (m_F=1/2). Radiative decay brings atoms back to the 2^3S state with well-defined branching ratios from the B_{17} sublevel (both by spontaneous and by stimulated emission, dashed lines in Fig. 2c) and from any other sublevel that may have been indirectly populated by collisions (green arrow and dotted lines in Fig. 2c).

The main difficulty that is met when modelling OP arises from the velocity dependence introduced by the combination of Doppler shifts and of the pump laser spectral profile. Atoms with a given velocity projection v_z along the OP light beam direction constitute a velocity class for which populations are coupled by OP rate equations where the contributions of absorption and emission of light are given by [8]:

$$\left.\frac{da_i}{dt}\right|_{\rm OP} = \gamma\sum\nolimits_{j=1}^{18} T_{ij}b_j + \sum\nolimits_{j=1}^{18}\gamma_{ij}(b_j - a_i) \tag{13}$$

$$\left.\frac{db_j}{dt}\right|_{\rm OP} = -\gamma b_j + \sum\nolimits_{i=1}^{6}\gamma_{ij}(a_i - b_j), \tag{14}$$

where γ=1.022×10^7 s^{-1} is the radiative decay of the 2^3P state, T_{ij} is the transition matrix element, and γ_{ij} is the velocity-dependent OP rate of the transition $A_i \rightarrow B_j$. The OP rate γ_{ij} also depends on position $\mathbf{r}$ in the cell due to the transverse intensity profile of the pumping beam and to absorption along the beam path. For the case of a broadband laser of Gaussian linewidth L and intensity $I(\mathbf{r})$ tuned to the centre of the Doppler absorption profile, the OP rate at low pressure is given by:

$$\gamma_{ij}(v_z,\mathbf{r}) = \sqrt{\pi}I(\mathbf{r})T_{ij}\frac{\alpha f}{m_{\rm e}\omega_{ij}L}\exp\left[-\left(\frac{Dv_z}{L\bar{v}}\right)^2\right], \tag{15}$$

where α is the fine structure constant, f=0.5391 is the oscillator strength of the transition, $m_{\rm e}$ is the electron mass, $\omega_{ij}/2\pi$ is the frequency of the $A_i \rightarrow B_j$ optical transition, $\bar{v}=\sqrt{2k_BT/M_3}$ is the

[3] A more realistic description of the depolarising effect of collisions in the 2^3P state (involving relevant cross sections for electronic angular momentum changing collisions [29], conservation of nuclear spin, and hyperfine recoupling following each collision) exceeds the scope of this report and will be given elsewhere. We use here the simple single-rate phenomenological approach used in previous models [8, 24]. It is expected to allow meaningful discussion of pressure effects on quantum efficiencies of C_8 and C_9 OP lines that address the same 2^3P_0 level.

most probable speed (T is the temperature, M_3 the atomic mass of ^{3}He), and D=$(\omega_{ij}/2\pi)\bar{v}/c$ is the associated Doppler width. In the model, the local OP light intensity $I(\mathbf{r})$ is computed from the incident laser power $W_{\rm las}$ and from the beam profile, taking into account the local atomic absorption in a self-consistent iterative way (forward and back-reflected intensities are added up in case of double pass).

Solving sets of rate equations for various velocity classes would be a difficult task since their populations are coupled by velocity-changing and by ME collisions, with ill-known collision rates. Instead, a coarse description with as few as two broad velocity classes is used to account for the Maxwell distribution of atomic velocities in the pumped gas: strongly pumped atoms, in the centre of the velocity distribution (with e.g. $v_z/\bar{v} \leq L/D$), and weakly pumped atoms, in the wings of the velocity distribution. This is a crude model, however it is sufficient to capture the essential features of velocity-selective OP effects and it usually provides reliable quantitative results.

In high magnetic field MEOP is performed on one of the intense $\mathrm{f}_2^{\pm}$ or $\mathrm{f}_4^{\pm}$ absorption lines (see Fig. 4) that combine 2 or 4 components with matrix elements close to 1 and thus provide much higher OP rates than low-field C_8 or C_9 lines at given pump intensity. In high pressure situations, three elements of the model are modified: full collisional redistribution in the 2^3P state simplifies Eqs. 13 and 14; the Doppler atomic absorption profile has to be replaced by a broader Voigt profile, which modifies the expression of the OP rate of Eq. 15 and decreases its value; fast collisional redistribution between velocity classes occurs in the 2^3S state and reduces the velocity dependent effects of OP, that can be neglected even if single-frequency laser pump is used. The MEOP model, with fewer phenomenological parameters ($\gamma_{\rm r}^{\rm P}$ and the partition of velocity classes are dropped), can thus be expected to provide more robust results.

2.5. Computed solutions of the complete rate equations at low field

In this section we quantitatively discuss the case of low pressure and low field OP that corresponds to currently operating MEOP-based gas polarisers. Specific features of high field situations [31] exceed the scope of this contribution and will be fully discussed elsewhere.

Coupled rate equations for the populations in the 2^3S and 2^3P state are obtained adding up the contributions of ME, OP, and relaxation (Eqs. 5, 11 and 12, 13 and 14). Characteristic rates of evolution for these two states are set by $\gamma_{\rm e}$ and γ, while the time evolution of the nuclear polarisation in the ground state (Eq. 18 below) involves rates typically six orders of magnitude smaller (e.g., $\gamma_{\rm e} n_{\rm m}/N_{\rm g}$ for ME). The coupled rate equations are thus solved adiabatically, by computing (quasi-) steady-state solutions in the 2^3S and 2^3P states assuming fixed values of all parameters, including the nuclear polarisation M in the ground state.

The effect of the competition between ME and OP is illustrated in Fig. 5 that displays the six populations of strongly pumped atoms in the 2^3S state for M=0 and M=0.5, in the absence of relaxation in the 2^3S state ($\gamma_{\rm r}^{\rm S}$=0). In the absence of OP spin-temperature populations are obtained, as expected (see Sec. 2.2): all populations are equal to 1/6 for M =0 and adjacent populations (for sublevels with $m'_F - m_F$=1) have a constant ratio for $M \neq$0 (e.g., 3 for M=0.5). With the example of OP conditions chosen in Fig. 5 (double pass C_8 pumping with about 5 W/cm^2 of incident light intensity, yielding an effective pumping rate of order 4.8γ for the strongly pumped atoms), the addressed sublevel A_5 is efficiently depleted. All other sublevel populations are affected as well by the combined effects of 2^3P radiative decay paths in the OP cycle (see, e.g., Fig. 2c) and of hyperfine recoupling following ME collisions. In the 2^3P state, with the same MEOP conditions, the computed populations are b_{17}/a_5=0.77 for the radiatively populated level and b_j/b_{17}=0.023 for the other levels (that are populated by collisions).

Such modifications of populations with respect to the spin-temperature distribution strongly affect the way resonant light is absorbed. The pump light absorption, that depends on the difference of populations of the involved sublevels (a_5-b_{17} in the case of Fig. 5), significantly

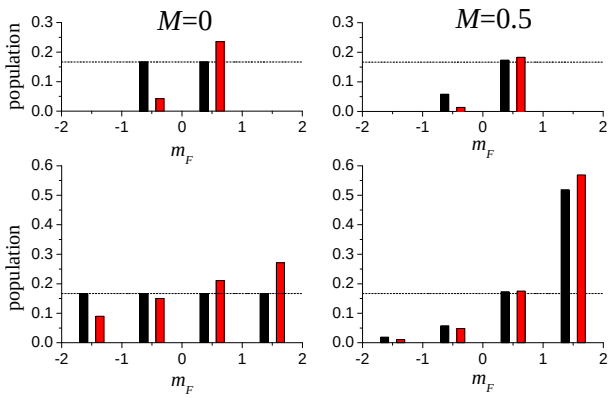

Figure 5. Computed populations in the 2^3S state for strongly pumped ^{3}He atoms at B=1 mT, for two values of M. Upper plots: populations a_5 and a_6 (F=1/2); lower plots: populations a_1 to a_4 (F=3/2). Black (left) bars: ST populations in the absence of OP. Red (right) bars: example of modified populations for strongly pumped atoms in a 1.33 mbar gas on the axis of the Gaussian pump beam (C_8 σ_+ pumping, $W_{\rm las}$=5 W, 1.33 cm fwhm diameter, 1.7 GHz fwhm spectral width; uniform $n_{\rm m}$= $10^{-6} \times N_{\rm g}$=3.2×10^{10} at/cm^3; $l_{\rm path}$ =2×30 cm).

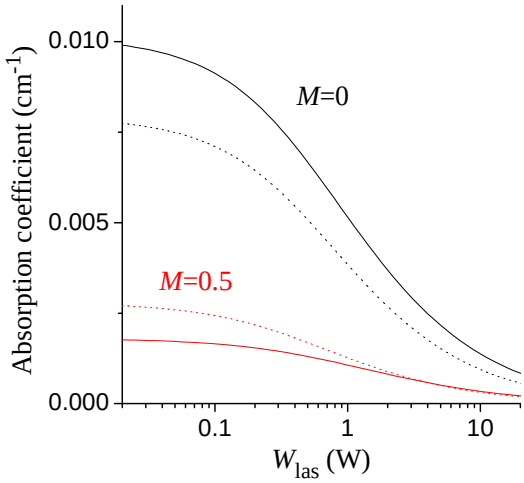

Figure 6. Overall pump absorption coefficients at M=0 (upper black curves) and M=0.5 (lower red curves) for C_8 (dotted lines) and C_9 (solid lines) OP, computed as a function of incident power $W_{\rm las}$ (same conditions as in Fig. 5).

decreases both with increasing M and with increasing pumping rate. This is illustrated in Fig. 6, in which the overall pump light absorption coefficient, -ln $T_{\rm pump}/l_{\rm path}$, is displayed as a function of pump power ($T_{\rm pump}$ is the computed pump transmittance for the absorbing gas, $l_{\rm path}$ is twice the cell length in the double-pass configuration). Computations are made for parameters corresponding to typical conditions of the experiments reported in the next section. Overall transmittance $T_{\rm pump}$ is computed by averaging over the transverse beam profile and over the two broad velocity classes. At fixed M, absorption significantly decreases at high light intensity: it is halved for $W_{\rm las}$=1 W in these conditions and would decrease more rapidly for a spectrally narrower laser or for a geometrically less expanded beam. Since it depends on $\gamma_{ij}/\gamma_{\rm e}$, the departure from the spin-temperature distribution under the influence of OP occurs at lower intensities for lower gas pressures. Fig. 6 also shows that the pump absorption decrease observed for increasing polarisation at fixed OP power is different for C_8 and C_9 lines.

An important consequence of the redistribution of populations by the intense OP light concerns the applicability of optical detection methods based on absorption measurements of a 1083 nm probe beam [24]. M can be accurately inferred from measurement of populations in the 2^3S state when a spin-temperature distribution prevails. An experimental study of the influence of OP-induced population changes on such optical methods is reported in a companion contribution in the same conference proceedings [32].

3. Photon efficiency and angular momentum budget

Numerical computation of all populations in the 2^3S and 2^3P states is indeed sufficient to fully characterise both the effect of OP on the electronic and nuclear orientations and on the absorption of light by the gas. However, it is useful for the sake of discussion to separately consider the angular momentum transfer from OP light to atomic variables, the effects of

relaxation on the atomic angular momentum in each state, and the flow of angular momentum associated with ME collisions.

As was briefly mentioned in the discussion of the OP cycle (section 2.4 and Fig 2c), the net change of atomic angular momentum projection $m_{\rm F}$ upon the absorption and emission of a photon, that we call the OP photon efficiency (PE) η, depends on several factors. In all situations PEs depend on the magnetic field through ratios of transition intensities. For any transition addressing a single Zeeman sublevel of the 2^3S state, the PE does not depend on nuclear polarisation nor on OP intensity. This occurs for the C_8 line of ^{3}He and the D_0 line of ^{4}He at low field, and also for several high-field transitions. For the D_0 line, the PE additionally does not depend on pressure.

For C_8, η only depends on the relaxation rate in the 2^3P state:

$$\eta_{\rm C8} = \frac{\gamma\eta^{\rm K}_{\rm C8} + \gamma^{\rm P}_{\rm r}\eta^{\rm D}_{\rm C8}}{\gamma + \gamma^{\rm P}_{\rm r}}, \tag{16}$$

where $\eta^{\rm K}_{\rm C8}$=0.896 is evaluated from transition intensities in the limiting case of low-pressure OP (discussed by Kastler [33]), i.e., when $\gamma^{\rm P}_{\rm r} \ll \gamma$ and $\eta^{\rm D}_{\rm C8}$=0.5 is evaluated in the opposite limiting case of depopulation OP (a high pressure regime discussed by Dehmelt [34]), i.e., when $\gamma^{\rm P}_{\rm r} \gg \gamma$.

For C_9 the overall PE is a weighted average of the efficiencies for absorption by the two 2^3S Zeeman sublevels addressed by the pump, hence it depends on the ratio of their populations that in turn depends both on M and on OP intensity. For instance, for σ_+ pump light the PE is higher (and larger than 1) for A_1 than for A_2. Furthermore, collisions in the 2^3P state enhance the PE in this case by increasing the final m_F value from -1/2 to 0 in the 2^3P state. This is illustrated in Fig 7 for the M-dependence of $\eta_{\rm C9}$ at low pump intensity. With the 3 : 1 ratio (at B=0) of transition intensities from A_1 and from A_2, the PE is higher (and enhanced by collisional redistribution in the 2^3P state) at low M where absorption by A_1 dominates. The situation is reversed above M=0.5, where a_2/a_1=3 just compensates for the ratio of transition probabilities. Fig. 8 displays the power dependence of $\eta_{\rm C9}$ at fixed polarisations M=0 and M=0.5.

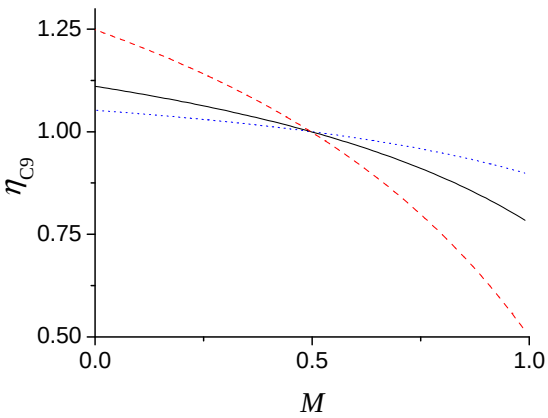

Figure 7. Computed M-dependence of the PE $\eta_{\rm C9}$ in the limit of low-intensity OP on the C_9 line. Red (dashed) line: $\eta^{\rm D}_{\rm C9}$, high pressure limit; black (solid) line: 1.33 mbar, intermediate collisional regime; blue (dotted) line: $\eta^{\rm K}_{\rm C9}$, low pressure limit.

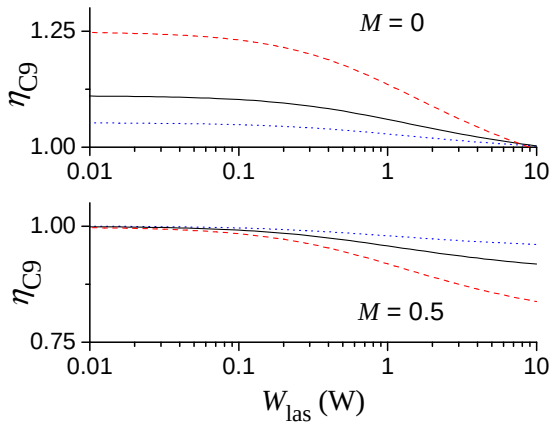

Figure 8. Computed power dependence of the PE of the C_9 line at M=0 (upper graph) and M=0.5 (lower graph) for the same three collisional regimes as in Fig. 7. $\eta_{\rm C9}$ is here the spatial average of the PE in the cell, computed for the same pump beam parameters as in Fig. 5.

In high field the $f_2^{\pm}$ and OP lines $f_4^{\pm}$ consist, like C_9, of several components having different individual PEs. As a result their overall PEs also depend on M and on OP light intensity. They are additionally sensitive to laser light detuning from the centre of the composite pump line. For instance, at M=0 and low pump intensity the PEs are computed, and have been checked [31, 35], to be of order 1 for the $f_2^{\pm}$ lines and 0.5 for the $f_4^{\pm}$ lines. The PEs can be significantly increased by detuning the pump laser away from the less efficient component(s). This is also the case at finite M and for any pump power, which accounts for the higher OP performance systematically obtained in experiments with an appropriately detuned pump laser [31].

As regards the ground state, the contribution of ME collisions to the rate equation describing the evolution of M is obtained by computing $\mathrm{Tr}_n\, \rho_g I_z$ using Eqs. 3 and 4:

$$\left.\frac{dM}{dt}\right|_{\mathrm{ME}} = \gamma_{\mathrm{e}} \int_{\mathrm{cell}} \frac{d^3\mathbf{r}}{V_{\mathrm{cell}}} \frac{n_{\mathrm{m}}}{N_{\mathrm{g}}} \left(\langle I\rangle_{\mathrm{m}} - M\right), \quad \text{where} \quad \langle I\rangle_{\mathrm{m}} = \sum_{k=1}^{6} L_k a_k. \tag{17}$$

The nuclear polarisation is uniform in the ground state since relevant diffusion rates in a low pressure gas are usually much larger than typical rates of evolution for M. However both the nuclear polarisation $\langle I\rangle_{\mathrm{m}}$ and the metastable density n_{m} can strongly vary over the volume of the cell, hence Eq. 17 involves a spatial average over the cell volume. Using (L_k)=(-1, L_-, L_+, 1, $-L_-$, $-L_+$),[4] where the field-dependent parameters $L_{\pm}$=$\cos^2\theta_{\pm} - \sin^2\theta_{\pm}$ can be evaluated from the 2^3S state mixing parameters θ_- and θ_+ [24], the nuclear polarisation $\langle I_z\rangle_{\mathrm{m}}$ in the metastable state is directly derived from the computed populations. For B=0, the coefficients are $L_{\pm}$=$\pm 1/3$. In high fields they weakly differ from 1, which reduces the flow rate of angular momentum: a large number of ME collisions is required to transfer a unit of angular momentum between ground state and 2^3S state atoms [24, 35].

All other processes directly acting on the nuclear polarisation in the ground state tend to drive it to its (quasi-) null thermal equilibrium value with a relaxation rate Γ_{g}. The total rate equation for the nuclear polarisation of ground state atoms is thus given by:

$$\frac{dM}{dt} = -\Gamma_{\mathrm{g}} M + \left.\frac{dM}{dt}\right|_{\mathrm{ME}}. \tag{18}$$

The skewing of the distribution of populations enforced by OP (see Fig. 5) provides the driving term in the build-up of nuclear polarisation from an initially unpolarised state. Conversely, if OP is interrupted in a polarised gas, relaxation in the 2^3S state induces a loss of angular momentum that has to flow from the ground state reservoir of nuclear angular momentum. At low nuclear polarisation this loss is known to introduce for the ground state polarisation an additional decay with a rate Γ^0_{ME} such that [19]:

$$\left.\frac{dM}{dt}\right|_{\mathrm{ME}}^{(W_{\mathrm{las}}=0,\ M\ll 1)} = -\Gamma^0_{\mathrm{ME}} M, \quad \text{with} \quad \Gamma^0_{\mathrm{ME}} = \frac{11}{3} \int_{\mathrm{cell}} \frac{d^3\mathbf{r}}{V_{\mathrm{cell}}} \frac{n_{\mathrm{m}}}{N_{\mathrm{g}}} \gamma_{\mathrm{r}}^{\mathrm{S}}. \tag{19}$$

For an arbitrary polarisation M we introduce the factor f_Γ defined by:

$$\left.\frac{dM}{dt}\right|_{\mathrm{ME}}^{(W_{\mathrm{las}}=0)} = -f_\Gamma \Gamma^0_{\mathrm{ME}} M. \tag{20}$$

Polarisation decay in the plasma in the absence of OP is then described by:

$$\frac{dM}{dt}^{(W_{\mathrm{las}}=0)} = -\Gamma^{\mathrm{decay}} M, \quad \text{with} \quad \Gamma^{\mathrm{decay}} = \Gamma_{\mathrm{g}} + f_\Gamma \Gamma^0_{\mathrm{ME}}. \tag{21}$$

[4] This expression of the coefficients in (L_k) is valid up to B=0.1619 T; the same permutation of indices resulting from level crossings as in Eqs. 8 and 9 must be applied for higher field strengths.

Computed f_Γ is found to be insensitive to plasma parameters (n_m, N_g, $\gamma_\mathrm{r}^\mathrm{S}$) and to the magnetic field strength over a wide range of conditions. It universally decreases with polarisation and has the M^2 dependence plotted in Fig. 9. The impact of this variation is discussed in Sect. 4.2 for a typical experimental polarisation decay.

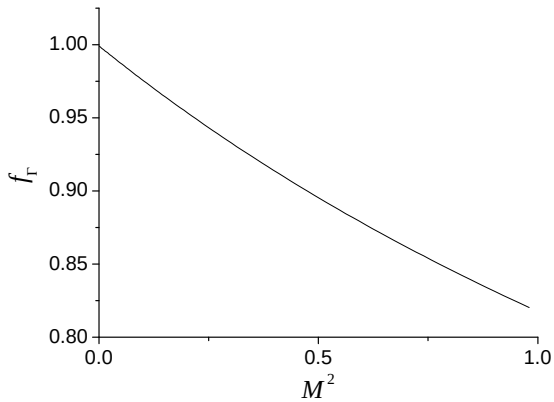

Figure 9. Computed decay rate factor f_Γ in Eq. 20 characterising the deviation of ME-induced decay of M from the small M regime of Eq. 19. The empirical fit f_Γ=0.999−0.2340M^2+0.0539M^4 is accurate to better than 4×10^{-4}.

When OP is applied and losses occur in the 2^3S state due to relaxation ($\gamma_\mathrm{r}^\mathrm{S} \neq 0$), part of the angular momentum deposited by the OP cycles is dissipated and the remainder is transferred to the ground state. When a single sublevel is addressed by the OP (hence the PE is a constant) one can write a formula that conveniently accounts for this polarisation loss at finite M. For instance, for OP on the C_8 transition in low field the ME contribution (Eq.17) is written as:

$$\left.\frac{dM}{dt}\right|_\mathrm{ME} = 2\eta_\mathrm{C8}\frac{(1-T_\mathrm{pump})\,W_\mathrm{las}}{N_\mathrm{g}V_\mathrm{cell}\hbar\omega_{ij}} - f'_\Gamma\Gamma^0_\mathrm{ME}M. \tag{22}$$

The first term on the right hand side of Eq. 22 corresponds to angular momentum conservation in the absence of relaxation ($\gamma_\mathrm{r}^\mathrm{S}$=0, hence Γ^0_ME=0): the number of flipped nuclei per unit time, $(N_\mathrm{g}V_\mathrm{cell}/2)\,dM/dt|_\mathrm{ME}$, is just equal to the product of the PE, η_C8, by the number of absorbed photons per unit time, $(1-T_\mathrm{pump})\,I_\mathrm{OP}/\hbar\omega_{ij}$. The choice of the form of the second term results from the fact that, for any distribution of populations resulting from the competition of ME, OP, and relaxation, the computed angular momentum loss in the 2^3S state is very close, over the whole range of experimental parameters, to the one contributing to polarisation decay in the absence of OP (Eq. 20). Neglecting the difference between f'_Γ and f_Γ leads to a useful alternative form of Eq. 18:

$$\frac{dM}{dt} = -\Gamma_\mathrm{R}M + 2\eta_\mathrm{C8}\frac{(1-T_\mathrm{pump})\,W_\mathrm{las}}{N_\mathrm{g}V_\mathrm{cell}\hbar\omega_{ij}}, \quad \text{where } \Gamma_\mathrm{R} = \Gamma_\mathrm{g} + f_\Gamma\Gamma^0_\mathrm{ME}. \tag{23}$$

The total polarisation loss rate, Γ_R, is the sum of the decay rate Γ_g (corresponding to relaxation processes directly acting on atoms in the ground state) and of the additional decay rate introduced by ME (Eq. 20, resulting from relaxation of populations in the 2^3S state).

At null polarisation the total loss term in Eq. 23 vanishes and the photon efficiency η_C8 (that does not depend on M) is very simply related to the growth rate of polarisation:

$$\eta_\mathrm{C8} = \frac{1}{2}\frac{dM}{dt}^{(M=0)}\frac{N_\mathrm{g}V_\mathrm{cell}\hbar\omega_{ij}}{\left(1-T_\mathrm{pump}^{(M=0)}\right)W_\mathrm{las}}. \tag{24}$$

Eq. 23 can thus be rewritten so as to relate the total loss rate Γ_R to directly measurable quantities:

$$\Gamma_\mathrm{R}M = \frac{1-T_\mathrm{pump}}{1-T_\mathrm{pump}^{(M=0)}}\frac{dM}{dt}^{(M=0)} - \frac{dM}{dt}. \tag{25}$$

This takes a simple form at steady-state polarisation $M^{\rm eq}$, where the total loss term exactly balances the angular momentum deposited by the OP photons:

$$\Gamma_{\rm R} M^{\rm eq} = \frac{1 - T_{\rm pump}^{(M=M^{\rm eq})}}{1 - T_{\rm pump}^{(M=0)}} \frac{dM}{dt}^{(M=0)} . \tag{26}$$

Given the various parameters appearing in the rate equations, the model indeed allows to directly compute the ME contribution to the time evolution of M (Eq. 17), hence the kinetics of polarisation growth (Eq. 18) and the steady-state value $M^{\rm eq}$, if the loss rate $\Gamma_{\rm g}$ is known. It also allows to compute pump beam transmission and photon efficiencies that can be directly compared to measurable quantities, for instance to ascribe a value to the pressure-dependent relaxation rate $\gamma_{\rm r}^{\rm P}$. Angular momentum budget considerations provide much less insight on the detailed mechanism of MEOP but they lead to very robust predictions about the link between pump light absorption and polarisation kinetics (independent of specific features of this MEOP model, such as the coarse treatment of velocity-dependent OP rates).

4. Experimental results

Several experiments devoted to the quantitative study of ^{3}He MEOP under various non-standard conditions have been performed in the recent years. We report here on selected results, mainly regarding nuclear relaxation, obtained using an intense pumping light in standard MEOP conditions (low gas pressure and low magnetic field) [30] and we compare them to results obtained combining high gas pressure and high magnetic field [13, 31, 35].

4.1. Experimental setup and polarisation measurement at low field

A dedicated setup, schematically described in Fig. 10, has been constructed to characterise MEOP kinetics and performance over a wide range of conditions encompassing the usual operating parameters of gas polarisers. An end-compensated solenoid provides a uniform

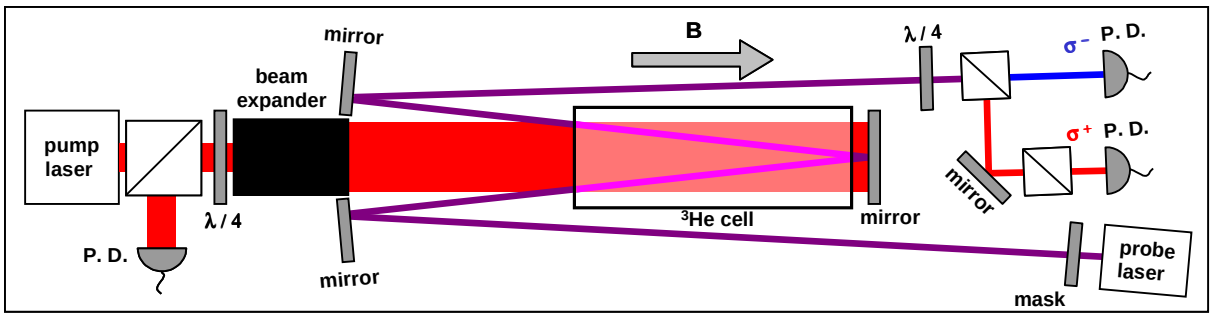

Figure 10. Schematic of the set-up used for low-field MEOP studies. Pump and probe laser lights are delivered to the experiment by single-mode fibres. The Gaussian pump beam is collimated by a f=7 cm lens, circularly polarised by a polarising beam splitting cube and a quarterwave plate ($\lambda/4$), and expanded to a diameter of 1.4 cm fwhm. The weak probe beam is split and polarised by a mask to obtain two vertically separated adjacent beams (this is not visible in this top view). The probe beams, with opposite circular polarisations, are separated by a circular analyser. Photodiodes (P.D.) are used to monitor the transmitted pump and probe beam powers after a double pass through the cell .

magnetic field (B=0−30 mT, mean $\Delta B/B$=50 ppm/cm) over the volume of the experimental cells. These are sealed cylindrical quartz cells (30 cm long, 6 cm in diameter) with optically

polished windows, filled with pure ^{3}He gas after a standard cleaning protocol. We report here on results of studies performed at B=1 mT for three gas pressures: 0.63, 1.19, and 2.45 mbar. A rf discharge is sustained in the cell using two sets of alternating wire electrodes connected to a voltage transformer tuned to the rf frequency (of order 2 MHz). Partial amplitude modulation of the rf power (around 70 Hz) and lock-in detection are used to improve the sensitivity of the absorption measurements. For most experiments, a broadband 1083 nm fibre laser provides the OP pump power (Keopsys, 5 Watt model, 1.7 GHz fwhm). For enhanced OP efficiency the light is back-reflected for a second pass through the cell. After deflection by the circular polariser, the transmitted light is monitored for measurements of the absorbed pump power. A longitudinal optical detection method is used to measure the nuclear polarisation in the gas during experiments [32]. It is based on absorption measurements of two weak probe beams (provided by a 1083 nm DBR diode) arranged in a W-shaped path for convenience (see Fig. 10), having complementary σ_+ and σ_- circular polarisations separately monitored using two photodiodes.

Examples of demodulated and processed signals obtained from the recordings of the photodiode output voltages are displayed in figure 11 for C_8-σ_+ OP experiments where short periods of polarisation build-up alternate with periods with a blocked pump. The upper graphs

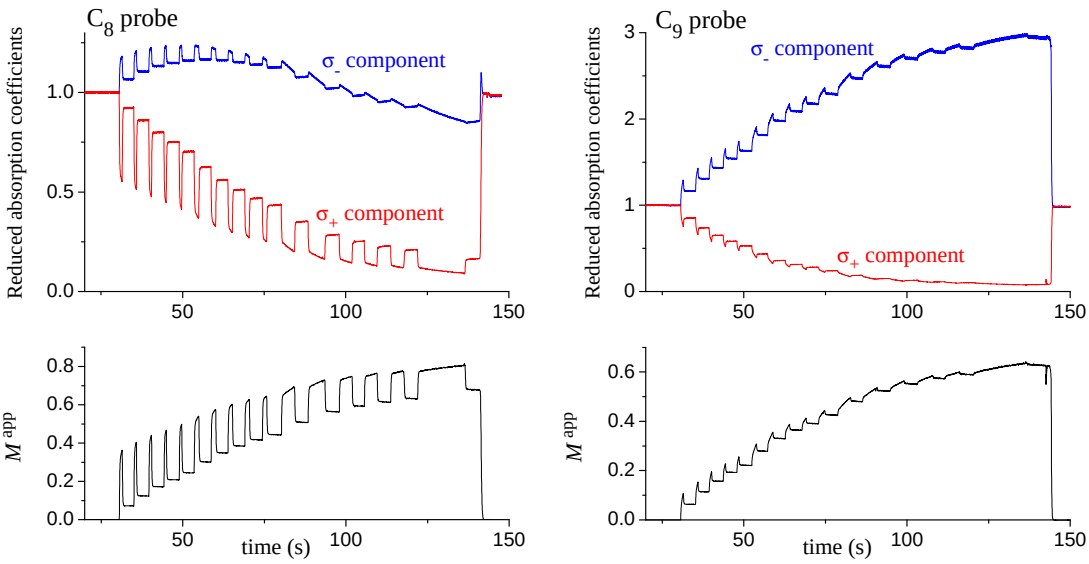

Figure 11. Two processed time recordings obtained from probe photodiode voltages for the 1.19 mbar cell. Left (resp., right) graphs: the probe laser is tuned to C_8 (resp., C_9). Both recordings are made with the OP beam (σ_+-polarised, tuned to C_8, $W_{\rm las}$=1.55 W) alternatively applied and blocked. Upper graphs: reduced absorption coefficients are computed from demodulated photodiode voltages (see Sec. 3.5 in [32]). Lower graphs: time evolutions of the apparent polarisations $M^{\rm app}$ are computed from the signals in the upper graphs using Eqs. 3 and 5 of [32]. When the pump is blocked $M^{\rm app}$ is equal to the ground state polarisation M. When the pump is applied the instant increase in $M^{\rm app}$ reveals the departure from a spin-temperature situation and the overpolarisation of the 2^3S state. This increase is larger when the pump and the probe address the same Zeeman sublevels (left versus right bottom graphs).

display reduced absorption coefficients (-ln T/-ln $T^{(M=0)}$) of the probe beams. Initially M=0 and both components are equally absorbed. Then, during the polarisation build-up, the absorption of the σ_+-polarised beam steadily decreases because of the decrease of the populations of sublevels with m_F<0 (a_1, a_2, and a_5). Additional transient decrease of absorption is observed whenever the

pump light is applied, which results from the strong distortion of the distribution of populations by intense OP (see Fig. 5). The sublevel A_5 is the most depleted and the 2^3P sublevel B_{17} is the most populated by the pump light. Probe light absorption is thus strongly decreased for the σ_+ component of the C_8-tuned probe beam, and much less for the σ_+ component of the C_9-tuned probe beam. Conversely, OP light and growing polarisation both tend to overpopulate sublevels with m_F>0 and thus to enhance the absorption of the σ_--polarised probe beam light. After reaching a maximum, absorption of the C_8 probe light would vanish at M=1 while absorption of the C_9 probe light would be enhanced by a factor of 4.5 compared to M=0.

These data provide a clear manifestation of the spin-temperature enforced distribution of populations in the absence of OP and of the overpolarisation induced by the pumping light in the 2^3S state. Similar recordings have also been performed with the probe laser detuned from resonance in order to address atoms of different velocity classes. This can be used to obtain quantitative information on velocity-selective OP effects and to evaluate the relevance and the limitations of the simple two-class model introduced in Section 2.4.

The lower graphs in Fig. 11 display the apparent polarisations $M^{\rm app}$ computed from the ratios of reduced absorption signals by assuming a spin-temperature distribution of populations (Eqs. 8 and 9). They show sawtooth patterns, with rising $M^{\rm app}$ (always overestimating the growing M) when the OP light is applied and decaying M when the OP beam is blocked. Such sets of data are used to accurately relate $M^{\rm app}$ to M for given OP conditions and choice of probe line. They are also used to test the MEOP model. Comparison to the computed apparent polarisations is quite satisfactory, with for instance a difference between computed and measured $M^{\rm app}$ values that do not exceed 0.015 for these experiments.

4.2. Characterisation of build-up and decay of polarisation

A standard MEOP experiment consists in monitoring transmitted pump and probe beam powers for selected rf intensity for the discharge, OP power and line, and probe laser line (C_8 or C_9). A typical recording of polarisation build-up and decay is displayed in Fig. 12.

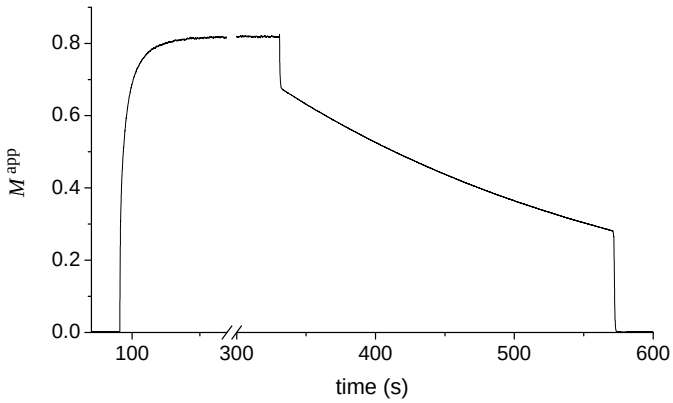

Figure 12. Time evolution of the apparent polarisation $M^{\rm app}$ in the 1.19 mbar cell, monitored using a C_8-tuned probe. OP is applied from t=91 s to t=330 s (C_8 line, $W_{\rm las}$=1.55 W). At t=570 s, the remaining polarisation is suddenly destroyed by enhanced nuclear relaxation (obtained by placing a small magnet close to the cell).

The build-up part is best discussed using Fig. 13a, in which the true polarisation M is inferred from $M^{\rm app}$ by applying the empirical correction function determined from the dedicated measurement of $M^{\rm app}$-M in the same OP conditions (Fig. 11). The difference of M to the equilibrium polarisation $M^{\rm eq}$=0.67 that is reached in steady-state in this experiment is plotted in semi-log scale (Fig. 13a). Departure from a straight line reveals a non-exponential approach of M towards $M^{\rm eq}$, systematically observed at low magnetic fields. The changing slope of the curve corresponds to a build-up rate $\Gamma_{\rm build}$=$(dM/dt)/(M^{\rm eq}$-$M)$ that decreases while M grows towards $M^{\rm eq}$. Fig. 13b displays values of dM/dt inferred from a running fit of the polarisation data. It is not a straight line and the local slope ($\Gamma_{\rm build}$, data not shown) is found to decrease

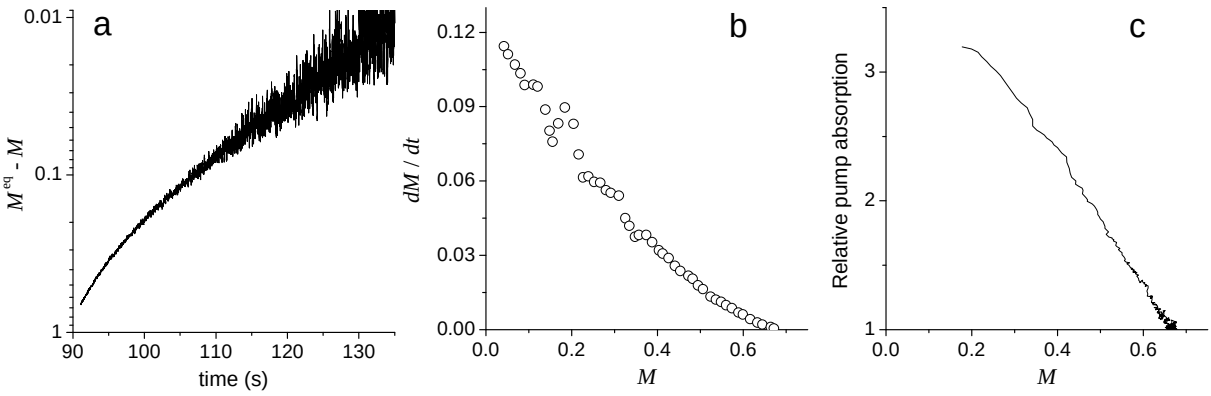

Figure 13. Analysis of polarisation build-up for the experiment displayed in Fig. 12. **a:** The difference of the true polarisation M to its steady-state value M^{eq} is plotted in a reversed semi-log scale as a function of time. The build-up is clearly non-exponential. **b:** The time derivative of M, inferred from local exponential fits to data, is plotted as a function of M. Extrapolation at M=0 provides $dM/dt^{(M=0)}$=0.125 s^{-1} **c:** Relative pump light absorption is plotted as a function of M. For convenience, the data are here normalised to the value reached at M=M^{eq}, where a transient switching off of the rf discharge (during the axis break in Fig. 12) is used to measure absolute pump and probe transmittances.

with M quite linearly, from 0.19 s^{-1} at M=0 to 0.06 s^{-1} at M=M^{eq}. The absorbed pump power, that is simultaneously recorded in the experiment, is plotted in Fig. 13c as a function of the polarisation. Due to the time constant set for high signal to noise ratio in this experiment, no meaningful absorption value is obtained during the first second of pumping. Still, pump absorption clearly decreases by a factor of order 4 when M increases from 0 to M^{eq}.

The decay part of the recording in Fig. 12 is best discussed using Fig. 14a, where decaying polarisation is plotted in semi-log scale. When the pump is blocked (after t=330 s), M^{app}=M can be accurately fit by an exponential function decaying to 0 (with a rms difference below 3×10^{-4}). This is a generic feature of polarisation decays in rf discharges, for which constant Γ^{decay} are obtained in all operating conditions and over a wide range of measured decay rates (10^{-4}–10^{-1} s^{-1}).

During decay a spin-temperature distribution of populations prevails and the populations are precisely known (Eqs. 8 and 9). The measured transmitted powers can thus be used to obtain the value of the metastable number density n_{m} (integrated along the probe path). Absolute transmittances are obtained only when the rf discharge is turned off but relative changes are reliably derived from demodulated signals at all times. This is used to obtain the data in Fig. 14b where the 2^3S number density n_{m} exhibits an approximate M^2-dependence during polarisation decay. The significant change in n_{m} (-15% when M decays from 0.67 to 0), that may for instance be attributed to the inhibiting effect of polarisation on Penning ionising collisions, induces an identical change of Γ^0_{ME} (Eq. 19) that is not compensated by the variation of the factor f_Γ (Fig. 9) in Eq. 21. The change in n_{m} also indicates that the plasma conditions are modified and suggests that Γ_{g} may vary with polarisation. Altogether, since Γ^{decay}=$\Gamma_{\mathrm{g}}+f_\Gamma\Gamma^0_{\mathrm{ME}}$, the precisely exponential character of decays recorded in very different experimental situations is puzzling and can certainly not be attributed to an accidental compensation for these independently varying quantities.

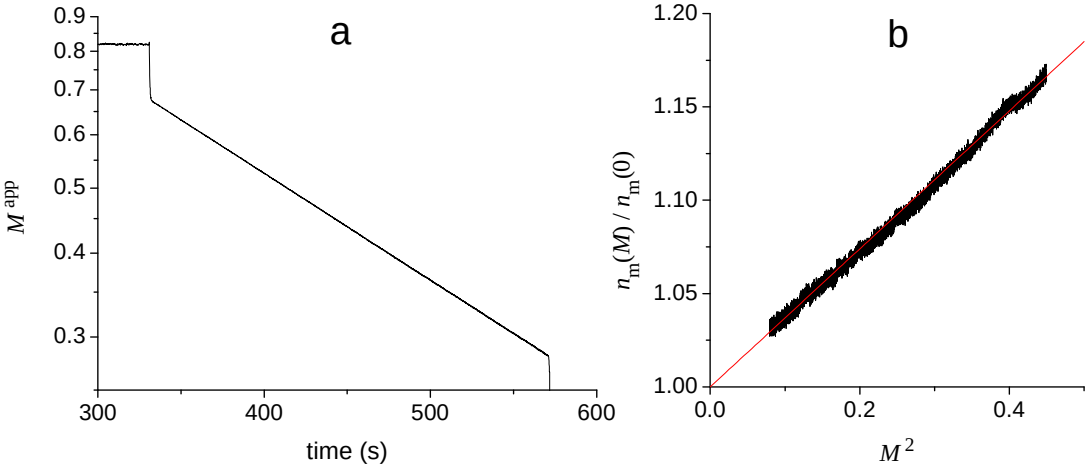

Figure 14. Analysis of polarisation decay for the experiment displayed in Fig. 12. **a:** $M^{\rm app}$, that reduces to M when the pump is blocked (after t=330 s), is plotted in a semi-log scale as a function of time. The decay is accurately exponential, with a rate $\Gamma^{\rm decay}$=3.667×10^{-3} s^{-1}. Extrapolation to t=330 s yields $M^{\rm eq}$=0.67. **b:** The relative change of the number density $n_{\rm m}$ of atoms in the 2^{3}S state is plotted as a function of M^2 for data taken during polarisation decay. The dotted line is a guide for the eye (slope: 0.37).

4.3. Steady-state polarisation and ground state nuclear relaxation

Steady-state nuclear polarisation $M^{\rm eq}$ is asymptotically reached when the ME contribution to the time evolution of M (Eq. 17) is just balanced by the direct relaxation term $-\Gamma_{\rm g}M$ in Eq. 18. Figure 15 displays computed values of this ME contribution for C$_8$ and C$_9$ OP and conditions corresponding to the recording of Fig. 12 ($W_{\rm las}$=1.55 W, p=1.19 mbar, probe transmittance T=0.48 at M=0, $\Gamma^{\rm decay}$=3.667×10^{-3} s^{-1}). For these calculations, 2^{3}S and ground

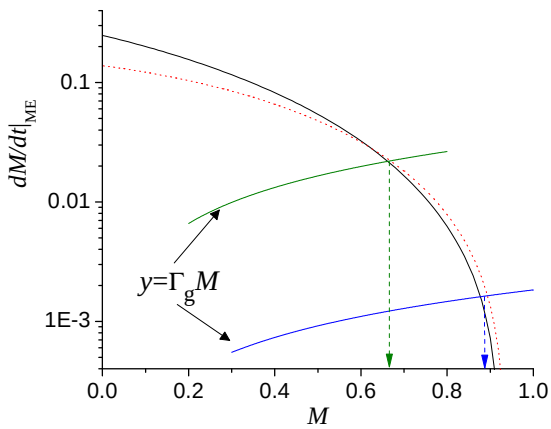

Figure 15. ME contributions to the evolution of M (Eq. 17) are computed as a function of M for OP on C$_9$ (solid black line) and C$_8$ (dotted red line) lines and plasma conditions specified in the text. The semi-log scale is used for convenient comparison of small values at large M. In this representation, the linear functions y=$\Gamma_{\rm g}M$ are not straight lines (upper curve: $\Gamma_{\rm g}$=0.033 s^{-1}; lower curve: $\Gamma_{\rm g}$=1.83×10^{-3} s^{-1}). The vertical arrows point at the corresponding steady-state values $M^{\rm eq}$ on the M-axis.

state relaxations are assumed to equally contribute to the measured polarisation decay of Fig. 14: $\Gamma^0_{\rm ME}$= $\Gamma_{\rm g}$=$\Gamma^{\rm decay}/2$. If one assumes, as usual, that nuclear relaxation of ground state atoms is not affected by the presence of the OP light, $M^{\rm eq}$ is graphically found to be of order 0.9 in Fig. 15 (at the crossing of the computed ME contribution with the lower of the two curves y=$\Gamma_{\rm g}M$). This value is found to be almost independent (±0.03 at most) of the chosen 2^{3}S relaxation rate,

provided that $\Gamma^0_{\rm ME}+\Gamma_{\rm g}=\Gamma^{\rm decay}$. It is much higher than the steady-state polarisation measured in the 1.19 mbar cell, $M^{\rm eq}$=0.67. This experimental value can be obtained at steady-state using the MEOP model only by assuming that $\Gamma_{\rm g}$ is much larger (here, 0.033 s^{-1}, corresponding to the upper of the two curves $y=\Gamma_{\rm g}M$) with the OP beam than without it .

Discrepancies are systematically obtained between experimental results and $M^{\rm eq}$ values computed with the MEOP model assuming that ground state relaxation is not affected by OP This is illustrated in Fig. 16 for a series of measurements in the other two cells used in this study. Computed results weakly depend on input parameters such as the spatial distribution of

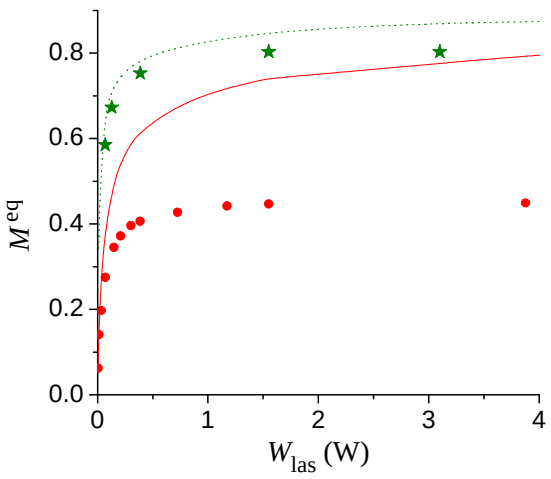

Figure 16. Measured (symbols) and computed (lines) values of the steady-state polarisations $M^{\rm eq}$ are plotted as a function of the incident pump power $W_{\rm las}$ for OP on C_8 in the 0.63 mbar cell (green stars and dotted line) and on C_9 in the 2.45 mbar cell (red circles and solid line). Computations are made for the parameters of the experiments ($n_{\rm m}$=1.1 and 4.2×10^{16} at/m^3 and $\Gamma_{\rm R}=\Gamma^{\rm decay}$= 2.9 and 13×10^{-3} s^{-1} at low and high pressure, corresponding to a weak and a rather intense discharge, respectively).

2^3S atoms in the cells, the relaxation rates $\gamma^{\rm S}_{\rm r}$ and $\gamma^{\rm P}_{\rm r}$, the OP laser spectral and geometrical profiles, etc. Assuming a significant, power-dependent increase of $\Gamma_{\rm g}$ during OP is the only way to reproduce experimental $M^{\rm eq}$ data with the MEOP model.

In the case of OP on the C_8 line, the angular momentum budget approach of Sec. 3 relating the total loss rate $\Gamma_{\rm R}$ introduced in Eq. 23 to directly measured quantities provides a model-independent and parameter-free approach to evaluate $\Gamma_{\rm R}$ during polarisation build-up (using Eq. 25) and at steady-state polarisation (using Eq. 26). When applied to the recording of Fig. 12 (C_8 pumping), Eq. 26 yields $\Gamma_{\rm R}$=0.047 s^{-1} at $M=M^{\rm eq}$. Given the uncertainties on the extrapolations at M=0 in Figs. 13b and 13c, this is in good agreement with the result obtained using the MEOP model for the Fig. 15 experiment where an OP-enhanced relaxation rate $\Gamma_{\rm R}$=0.0347 s^{-1} is required to account for the experimental observations. Here both inferred values of $\Gamma_{\rm R}$ are about 10 times higher than $\Gamma^{\rm decay}$.

When the angular momentum approach is applied to a full build-up recording to directly infer total loss rates from the measured pump transmittances and M growth rates (using Eq. 25) a time-dependent series of values for $\Gamma_{\rm R}$ is obtained that includes the value derived at $M^{\rm eq}$ as an end-point. Remarkably consistent sets of data are obtained when they are plotted as a function of the absorbed pump powers, as displayed in Fig. 17 that compiles the results from 13 C_8-pumping experiments performed at various incident pump powers in the three cells. At high pump powers all data collapse to a common line with $\Gamma_{\rm R}$ proportional to the absorbed power and OP-enhanced relaxation rates $\Gamma_{\rm R}$ reach values that are up to two orders of magnitude larger than $\Gamma^{\rm decay}$. At very low pump powers $\Gamma_{\rm R}$ would indeed recover the respective $\Gamma^{\rm decay}$ values measured in each cell for the chosen weak rf discharge level.

The full results of this study, performed for various discharge intensities and in fields up to 30 mT, will be reported elsewhere. They show a large and consistent increase of the ground state nuclear relaxation with the absorbed OP power. It is also worth comparing this with preliminary evidence of the same behaviour that has been obtained in MEOP studies at higher

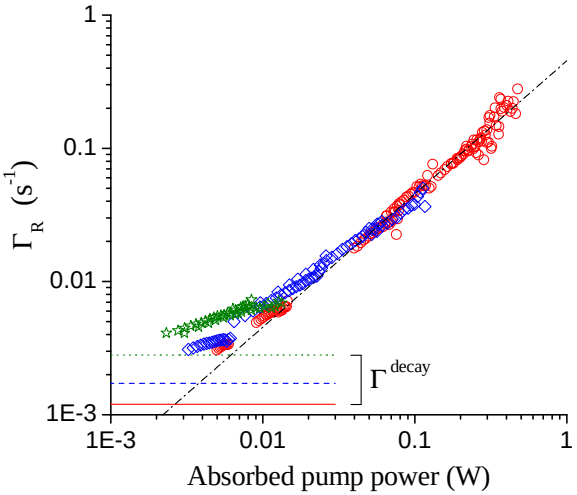

Figure 17. Examples of experimental total polarisation loss rates Γ_R obtained from polarisation build-ups (using Eq. 25) are plotted versus the absorbed OP power (C_8 pumping). The horizontal lines correspond to the measured Γ^{decay} values. Green stars and dotted line: 0.63 mbar; blue diamonds and dashed line: 1.19 mbar; red circles and solid line: 2.45 mbar. The dash-dotted line (y=x/2.2) is a guide for the eye.

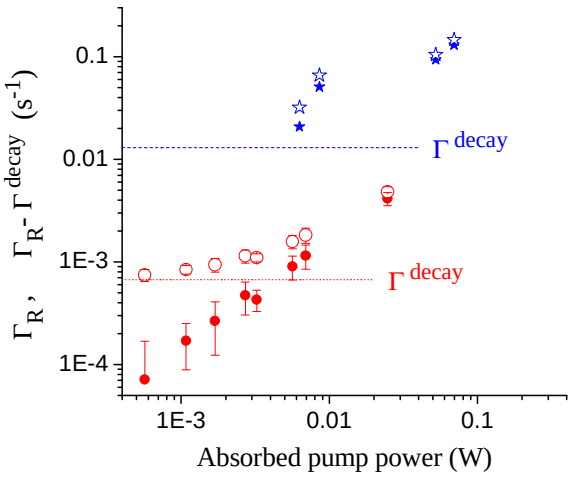

Figure 18. Total polarisation loss rates Γ_R (open symbols) for various absorbed OP powers in a 32 mbar cell, reproduced from Fig. 6.21 of [31]. The horizontal lines correspond to the measured Γ^{decay} values. The filled symbols are the differences Γ_R-Γ^{decay} plotted in the original figure. Blue stars and dashed line: B=3 mT, C_9 pump; red circles and dotted line: B=1.5 T, f_2^- pump.

gas pressures and applied fields [13, 35]. Figure 18, adapted from Fig. 6.21 of [31], displays Γ_R values inferred from the comparison of measured and computed M^{eq} data in a 32 mbar 5 cm×5 cm cell (using the MEOP model as shown in Fig. 15). At this pressure, MEOP is quite inefficient at low field (M^{eq}=0.11 with 2 W OP on the C_9 line at 3 mT) where rather large decay rates are measured (here, Γ^{decay}=13×10^{-3} s^{-1}), even for weak rf discharges. Still, OP-enhanced relaxation is observed and results are consistent with those presented in Fig. 17 if the appropriate cell length scaling is applied. Another striking feature is that high-field MEOP, which operates quite efficiently (M^{eq}=0.56 with 0.5 W OP at 1.5 T in the same cell) and with reduced decay rates (here, Γ^{decay}=0.67×10^{-3} s^{-1}), also gives rise to a strong OP-light-enhanced relaxation. This is currently being investigated at still higher pressures and magnetic field in Cracow [14, 15, 36].

5. Concluding remarks

We have described the main features of a comprehensive model that has been developed to account for the detailed features of MEOP in ^{3}He and in isotopic mixtures over a broad range of experimental conditions regarding field strength, gas pressure, pump laser intensity, and spectral characteristics. Selected results have been presented to illustrate the satisfactory agreement obtained bewteen computed and experimental data. The model has a limited number of free parameters and can be used for quantitative predictions of MEOP performance in gas polarisers (polarisations, growth rates, and magnetisations, with or without gas flow in OP cells) when reliable input values are available.

The model is used as a unified frame to understand, for instance, the surprisingly good MEOP results obtained in very high magnetic fields in spite of the strong hyperfine decoupling

that tends to impede the transfer of angular momentum from the absorbed polarised light to the ^{3}He nuclei. The same high photon efficiency (of order 1) is obtained at all field strengths, which is a key factor in a global angular momentum budget. Since lower nuclear relaxation rates are obtained when a high field is applied to a rf discharge, in particular at high gas pressures where ME collisional couplings are advantageously increased, this high photon efficiency provides high nuclear polarisations over a broader range of operating conditions, hence of potential applications of the MEOP technique.

Consistent experimental observations of strongly OP-enhanced polarisation loss rates, quantitatively inferred from the measured MEOP dynamics using the model or the angular momentum budget approach, provide solid evidence of a new nuclear relaxation process. The additional loss rates account for the surprising experimental fact that the achieved steady-state polarisations hardly increase when higher pump powers are used, in spite of higher pumping rates. Search for the physical origin of this light-induced relaxation that occurs at low and high field strengths is under way, with dedicated optical tools used to probe plasma changes during MEOP. Finding ways to alleviate this limiting relaxation problem could open the way to improved performance of the MEOP technique, both in terms of record polarisations and of increased throughput for gas polarisers.

References

[1] Colegrove F D, Schearer L D and Walters G K 1963 *Phys. Rev.* **132** 2561–2572

[2] Schearer L D 1969 *Physical Review* **188** 505 ISSN 0031-899X

[3] Lefevre-Seguin V and Leduc M 1977 *Journal of Physics B: Atomic and Molecular Physics* **10** 2157–2164 URL `http://dx.doi.org/10.1088/0022-3700/10/11/016`

[4] Xia T, Morgan S W, Jau Y Y and Happer W 2010 *Phys. Rev. A* **81** 033419 URL `http://pra.aps.org/abstract/PRA/v81/i3/e033419`

[5] Bouchiat M A, Carver T R and Varnum C M 1960 *Phys. Rev. Lett.* **5** 373–375

[6] Happer W 1972 *Rev. Mod. Phys.* **44** 169–249

[7] Chen W C, Gentile T R, Walker T G and Babcock E 2007 *Phys. Rev. A* **75** 013416 URL `http://link.aps.org/abstract/PRA/v75/e013416`

[8] Nacher P J and Leduc M 1985 *Journal de Physique* **46** 2057–2073 URL `http://dx.doi.org/10.1051/jphys:0198500460120205700`

[9] Mueller R 2001 *Physica B: Condensed Matter* **297** 277–281 ISSN 09214526 URL `http://dx.doi.org/10.1016/S0921-4526(00)00841-3`

[10] Gentile T, Hayden M and Barlow M 2003 *J. Opt. Soc. Am. B* **20** 2068–2074 URL `http://dx.doi.org/10.1364/JOSAB.20.002068`

[11] Tastevin G, Grot S, Courtade E, Bordais S and Nacher P J 2004 *Applied Physics B: Lasers and Optics* **78** 145–156 URL `http://dx.doi.org/10.1007/s00340-003-1325-1`

[12] Nacher P J, Courtade E, Abboud M, Sinatra A, Tastevin G and Dohnalik T 2002 *Acta Physica Polonica B* **33** 2225–2236 URL `http://hal.archives-ouvertes.fr/hal-00002223/`

[13] Abboud M, Sinatra A, Maitre X, Tastevin G and Nacher P J 2004 *EPL (Europhysics Letters)* **68** 480–486 URL `http://dx.doi.org/10.1209/epl/i2004-10237-y`

[14] Nikiel A, Palasz T, Suchanek M, Abboud M, Sinatra A, Olejniczak Z, Dohnalik T, Tastevin G and Nacher P J 2007 *European Physical Journal - Special Topics* **144** 255–263 ISSN 1951-6401

[15] Nikiel A *in preparation*

[16] Greenhow R C 1964 *Phys. Rev.* **136** A660–A662

[17] Daniels J, Timsit R, May A and Yuen V 1971 *Canadian Journal Of Physics* **49** 517 ISSN 0008-4204

[18] Daniels J and Timsit R 1971 *Canadian Journal Of Physics* **49** 525 ISSN 0008-4204

[19] Dupont-Roc J, Leduc M and Laloë F 1973 *Journal de Physique* **34** 961–976 and 977–987 ISSN 0302-0738 URL `http://dx.doi.org/10.1051/jphys:019730034011-12096100` and `http://dx.doi.org/10.1051/jphys:019730034011-12097700`

[20] Leduc M, Nacher P J, Tastevin G and Courtade E 2000 *Hyperfine Interactions* **127** 443–449 URL `http://dx.doi.org/10.1023/A:1012621818591`

[21] Wolf M 2004 *Erzeugung höchster 3He Kernspinpolarisation durch metastabiles optisches Pumpen* Ph.D. thesis Johannes Gutenberg-Universität Mainz URL `http://nbn-resolving.de/urn/resolver.pl?urn=urn:nbn:de:hebis:77-6554`

[22] Stoltz E, Meyerhoff M, Bigelow N, Leduc M, Nacher and Tastevin G 1996 *Applied Physics B: Lasers and Optics* **63** 629–633 URL http://dx.doi.org/10.1007/BF01831004
[23] Larat C 1991 *Laser LNA de puissance, application au pompage optique de l'hélium-3 et des mélanges hélium-3/hélium-4* Ph.D. thesis UPMC-Paris6 URL http://tel.archives-ouvertes.fr/tel-00011879
[24] Courtade E, Marion F, Nacher P J, Tastevin G, Kiersnowski K and Dohnalik T 2002 *The European Physical Journal D - Atomic, Molecular, Optical and Plasma Physics* **21** 25–55 URL http://dx.doi.org/10.1140/epjd/e2002-00176-1
[25] Pinard M and Laloë F 1980 *Journal de Physique* **41** 799–818 ISSN 0302-0738 URL http://dx.doi.org/10.1051/jphys:01980004108079900
[26] Dupont-Roc J, Leduc M and Laloë F 1971 *Phys. Rev. Lett.* **27** 467–470
[27] Fitzsimmons W A, Lane N F and Walters G K 1968 *Phys. Rev.* **174** 193–200
[28] Schearer L D 1967 *Phys. Rev.* **160** 76–80
[29] Vrinceanu D, Kotochigova S and Sadeghpour H R 2004 *Physical Review A* **69** 022714+ URL http://dx.doi.org/10.1103/PhysRevA.69.022714
[30] Batz M 2011 *Metastability exchange optical pumping of ^{3}He in magnetic fields up to 30 mT: Systematic investigations of performances and relaxation mechanisms* Ph.D. thesis UPMC - Paris 6 and Johannes Gutenberg-Universität Mainz
[31] Abboud M 2005 *Pompage optique de l'hélium-3 à forte pression dans un champ magnétique de 1.5 Tesla* Thèse de doctorat Université Pierre et Marie Curie URL http://tel.archives-ouvertes.fr/tel-00011099/
[32] Talbot C, Batz M, Nacher P J and Tastevin G 2011 *J. Phys.: Conf. Ser.* **This volume** xxx
[33] Kastler A 1957 *J. Opt. Soc. Am.* **47** 460–465 URL http://dx.doi.org/10.1364/JOSA.47.000460
[34] Dehmelt H G 1957 *Phys. Rev.* **105** 1487–1489
[35] Abboud M, Sinatra A, Tastevin G, Nacher P and Maitre X 2005 *Laser Physics* **15** 475–479 ISSN 1054-660X
[36] Suchanek K, Suchanek M, Nikiel A, Palasz T, Abboud M, Sinatra A, Nacher P J, Tastevin G, Olejniczak Z and Dohnalik T 2007 *European Physical Journal - Special Topics* **144** 67–74 ISSN 1951-6401